# Self-Locking Degree-4 Vertex Origami Structures

**Hongbin Fang[1*], Suyi Li[2], and K.W. Wang[1]**

[1)] Department of Mechanical Engineering, University of Michigan, Ann Arbor, MI 48109, USA
[2)] Department of Mechanical Engineering, Clemson University, Clemson, SC 29634, USA

[*]**Author for correspondence:** hongbinf@umich.edu (H. Fang)

**Abstract:**

A generic degree-4 vertex (4-vertex) origami possesses one continuous degree-of-freedom for rigid folding, and this folding process can be stopped when two of its facets bind together. Such facet-binding will induce *self-locking* so that the overall structure stays at a pre-specified configuration without additional locking elements or actuators. Self-locking offers many promising properties, such as programmable deformation ranges and piecewise stiffness jumps, that could significantly advance many adaptive structural systems. However, despite its excellent potential, the origami self-locking features have not been well studied, understood, and utilized. To advance the state of the art, this research conducts a comprehensive investigation on the principles of achieving and harnessing self-locking in 4-vertex origami structures. Especially, for the first time, this study expands the 4-vertex structure construction from single-component to dual-component designs and investigates their self-locking behaviors. By exploiting various tessellation designs, this research discovers that the dual-component designs offer the origami structures with extraordinary attributes that the single-component structures do not have, which include the existence of flat-folded locking planes, programmable locking points and deformability. Finally, proof-of-concept experiments investigate how self-locking can effectively induce piecewise stiffness jumps. The results of this research provide new scientific knowledge and a systematic framework for the design, analysis, and utilization of self-locking origami structures for many potential engineering applications.

**Keywords:**

Facet-binding, piecewise stiffness, mechanical metamaterial, programmable structures

## 1 Introduction

Over the recent decades, the influences of origami—an ancient art of paper folding—have expanded deep into the field of science and engineering [1–3]. One reason behind such development is that the principles of folding can be translated into designs of sophisticated three-dimensional structures with various functionalities. Given that folding-induced mechanical properties are scale-independent, origami-inspired designs have been applied to applications with vastly different length scales: such as nano-scaled DNA origami [4], micro-scaled biomedical devices [2,5,6], macro-scaled printable robots [2,7,8], sandwich panels [9], actuators [10], and large-scaled aerospace [11] and architectural elements [1,12]. One of the recently emerging research topics is origami-based mechanical metamaterial [13–19]. By programming the constituent origami cells' geometry, kinematic and mechanical properties of the metamaterial can be tailored within a large design space; and some unorthodox characteristics like auxetic effects [14,15] and multistability [15,18,19] can be achieved. Most of the aforementioned examples are based on a particular subset of folding pattern called rigid-foldable origami, whose folding only involves crease hinge rotation without deforming the quadrilateral facets, so that origami can be made by relatively stiff materials for broad applications.

An interesting feature of rigid origami folding is "*locking*". When it occurs, the origami structure fixes at a particular configuration and cannot be folded further. There are various mechanisms that can cause locking. For example, undesired locking may happen if the facet thickness of rigid-origami is not negligible. Due to the facet thickness, the actual installed hinges may deviate from the ideal position and prevent folding by generating a locking state. In addition, the facets of thick origami can come into contact with each other and stop folding, even though the corresponding zero-thickness kinematic model does not predict any self-intersections. Typically, locking reduces the achievable range of folding so it is to be avoided. In the case of thick origami, different techniques have been suggested to regain the full range of folding [20–22]. On the other hand, in applications like self-deployable structures [11] and self-folding devices [2,6], prescribed and controllable locking becomes beneficial or even indispensable

because the ability to limit folding and to stay at a desired configuration is crucial. One way to achieve controllable locking is by introducing additional locker elements [9,23]. In some micro self-folding devices, self-aligned locking hinges made of solder were employed at the edges of origami panels [6,24]. These locking hinges functioned as a stabilizing stop to increase fault tolerance in folding and ensure pre-specified folding angles; they could also improve the mechanical strength of the structure and enhance the cooperativity during folding. Another method to achieve controlled locking is by utilizing active materials. For example, a combination of shape memory alloys (SMA) and shape memory polymers (SMP) could create a self-folding laminate with controllable locking ability [25,26]: the SMA functions as an actuator to generate folding deformation, while the SMP locks the achieved deformation.

Other than relying on additional locker elements or active materials, controllable locking can also be achieved by harnessing the intrinsic characteristics of origami folding. One particularly interesting locking mechanism is facet-binding [14]. In a generic degree-4 vertex origami, there can exist a binding fold that is capable of fully closing while others are not, so that the two facets astride this fold line will bind together and induce locking [27]. Such a locking mechanism is named as "*self-locking*" in this paper. Schenk et al. [14] demonstrated an example of self-locking structure by connecting two different Miura-ori units together: folding deformation of this structure can be stopped at a predetermined configuration. Compared to other locking mechanisms, self-locking from facet binding is promising due to its simplicity and reliability. However, other than the particular example reported in [14], there is a lack of comprehensive investigation on the design and properties of self-locking structures. Especially, given the richness of origami tessellation methods, there can be different designs to achieve self-locking, and the corresponding locking behavior and kinematic properties can be very diverse. Currently there is no fundamental understanding of these interesting topics.

Motivated by the potentials of self-locking structures as well as the aforementioned limitations in the current state of the art, the research reported in this paper will fully characterize the self-locking in degree-4 vertex (for short, 4-vertex) origami. The reason for focusing on

4-vertex origami is because it is the simplest pattern that can be periodically tessellated in three directions and possesses only one continuous degree-of-freedom (DoF) for folding [27]. The following fundamental but largely unaddressed questions will be answered: How to enrich the 4-vertex structure designs by incorporating multiple cells with different geometries? Which structures possess the self-locking ability and what is the corresponding locking behavior? How to program the self-locking structures' kinematic properties? How would the mechanical properties change when self-locking happen? Answering these questions could significantly advance the state-of-the-art knowledge on self-locking structures and facilitate their applications.

This paper is structured as follows: § 2 briefly reviews the geometry of 4-vertex cells. This is followed by the construction of 4-vertex origami sheets and stacked blocks in §3, where new design ideas that incorporate dual components are presented. §4 presents the principles of achieving self-locking, with a major focus on determining the facets that first bind during folding. In §5 and §7, we exhibit new kinematic attributes of the structures that originated from self-locking and examine how to tailor them. An experimental exploration on the structure stiffness before and after self-locking occurs is reported in §7. Finally, a brief summary concludes the paper.

## 2. Four-vertex origami geometry

### (a) Cell geometry

A generic 4-vertex (G-4) cell consists of four rigid parallelogram facets connected by four ideal creases that meet at a point; its geometry can be characterized by two length parameters $(a, b)$ and four sector angles $\alpha_i$ $(i=1,2,3,4)$, see figure 1*a*. To ensure developability and avoid triviality, we assume $\sum\alpha_i = 2\pi$ and $\alpha_j < \sum\alpha_{i\neq j}$ [27], which reduce the number of independent sector angles to three. A partially folded state of the cell can be described by the dihedral angles $\rho_i$ $(i=1,2,3,4)$ between adjacent facets; conventionally, $\rho_i \in (0,\pi)$ for "mountain" fold, $\rho_i \in (\pi,2\pi)$ for "valley" fold, $\rho_i = \pi$ for unfolded state, and $\rho_i = 0$ or $2\pi$ for fully-folded state. To facilitate the analysis, in this research we assume that fold 4 has the opposite type (say, "valley" fold) from the rest (i.e., $\rho_4$ is the unique fold, which calls for

$\alpha_1+\alpha_4<\pi$ [27]), and fold 1 is capable of fully closing to $0^\circ$ (i.e., $\rho_1$ is the binding fold). We remark that such assumption provides generality because it is always possible to map a 4-vertex design to such arrangement via rotation and reflection.

Note that the ideal rigid-foldable 4-vertex cell retains a one continuous degree-of-freedom for folding. Hence, based on spherical trigonometry the dihedral angles $\rho_i$ $(i=2,3,4)$ can be expressed as functions of $\rho_1$ [28]

$$\begin{aligned}
\rho_2 &= \arccos\left(\frac{\cos\alpha_1-\cos\alpha_2\cos\xi}{\sin\alpha_2\sin\xi}\right)+\arccos\left(\frac{\cos\alpha_4-\cos\alpha\cos\xi}{\sin\alpha_3\sin\xi}\right),\\
\rho_3 &= \arccos\left(\frac{\cos\xi-\cos\alpha_3\cos\alpha_4}{\sin\alpha_3\sin\alpha_4}\right),\\
\rho_4 &= \arccos\left(\frac{\cos\alpha_2-\cos\alpha_1\cos\xi}{\sin\alpha_1\sin\xi}\right)+\arccos\left(\frac{\cos\alpha_3-\cos\alpha_4\cos\xi}{\sin\alpha_4\sin\xi}\right),
\end{aligned} \tag{2.1}$$

where $\xi=\arccos(\cos\alpha_1\cos\alpha_2+\sin\alpha_1\sin\alpha_2\cos\rho_1)$.

In 4-vertex cells, geometry constraints can be applied on sector angles to generate non-generic 4-vertex cells. If $\alpha_1+\alpha_3=\alpha_2+\alpha_4$, the 4-vertex cell can be folded to a flat state; if $\alpha_1+\alpha_2=\alpha_3+\alpha_4$, the two creases $\rho_2$ and $\rho_4$ are collinear. Hence, based on whether possessing flat-foldability or single collinearity, the 4-vertex cells can be classified into 4 types (figure 1*b* and table 1) [29,30]: the G-4 cell cannot be folded flat nor has collinear folds; the general flat-foldable (GFF) cell possess flat-foldability; the single-collinear (SC) cell has a pair of collinear folds; and the Miura-ori cell possesses both characters. Note that each additional constraint reduces the number of independent sector angles by one.

**Table 1**. Geometry of 4-vertex cells.

| Type | Geometry constraints other than $\sum\alpha_i=2\pi$, $\alpha_j<\sum\alpha_{i\neq j}$ | Independent sector angles | |
|---|---|---|---|
| | | # | List |
| G-4 | / | 3 | $\alpha_1$, $\alpha_2$, $\alpha_4$ |
| GFF | $\alpha_1+\alpha_3=\alpha_2+\alpha_4$ | 2 | $\alpha_1$, $\alpha_4$ |
| SC | $\alpha_1+\alpha_2=\alpha_3+\alpha_4$ | 2 | $\alpha_1$, $\alpha_4$ |
| Miura-ori | $\alpha_1+\alpha_3=\alpha_2+\alpha_4$, $\alpha_1+\alpha_2=\alpha_3+\alpha_4$ | 1 | $\alpha_1$ |

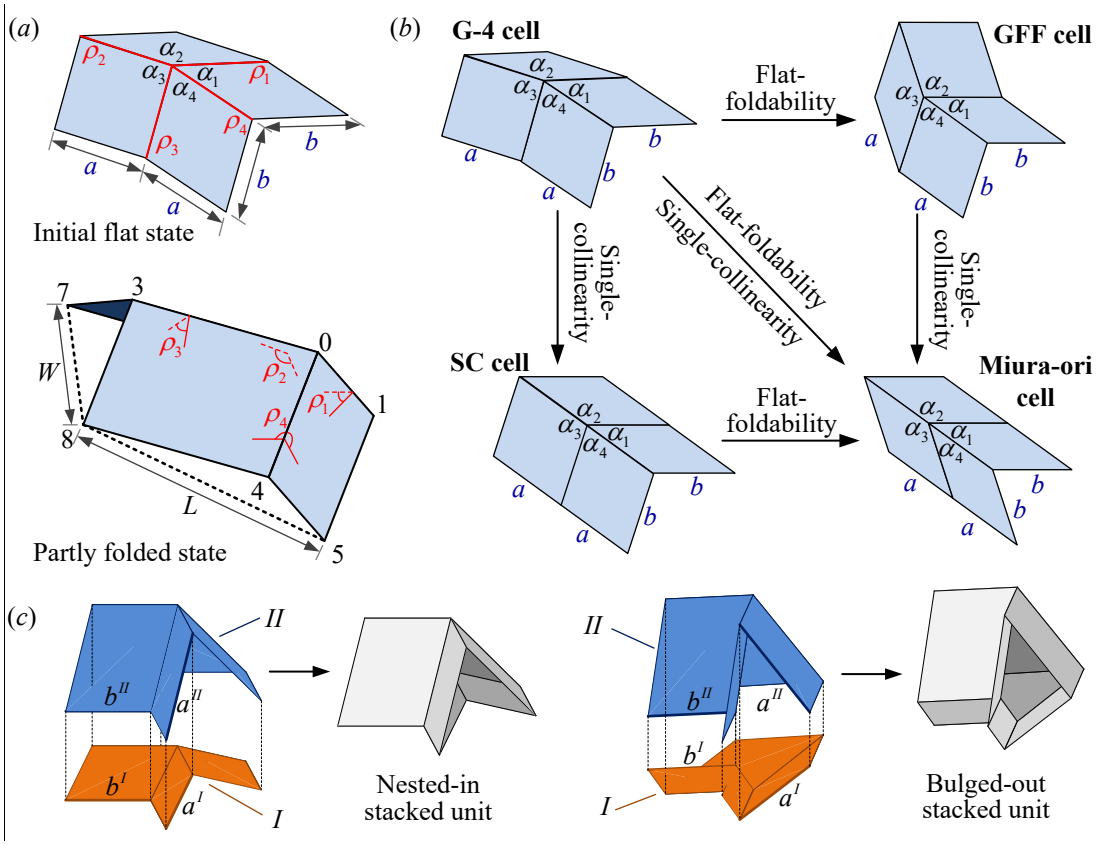


**Figure 1.** Four-vertex origami geometry. (*a*) Initial flat state and partly folded state of a G-4 cell. (*b*) Evolution among the G-4 cell and three types of non-generic 4-vertex cell. (c) Construction of the nested-in and bulged-out stacked units.

## (b) Stacking origami

Two 4-vertex cells of the same type but with different geometries are possible to be stacked along their zig-zag creases into a stacked unit, see figure 1*c*. During folding, the two cells should always be kinematically compatible so that they can keep connected at the zig-zag creases. Previous work [14,29] have derived the conditions for building GFF, SC, and Miura-ori stacked units, which are listed below for convenient use

$$b^{II} = b^{I},\ \frac{a^{I}}{a^{II}} = \frac{\cos\alpha_1^{II}}{\cos\alpha_1^{I}},\ \frac{\cos\alpha_1^{I}}{\cos\alpha_1^{II}} = \frac{\cos\alpha_4^{I}}{\cos\alpha_4^{II}}. \tag{2.2}$$

Here, the superscripts "*I*" and "*II*" denote the bottom cell and the top cell, respectively. For Miura-ori, the last equation in (2.2) is trivial [14]. We take $\alpha_1^{II}$ as the independent parameter of the top cell, and without loss of generality, we let $\alpha^{II} \geq \alpha^{I}$ so that the bottom cell can be either

nested into the top cell or bulged out from the top cell, corresponding to two topologically different configurations. Note that such stacked unit remains a single degree of freedom for folding, because the folding angles of the top cell can be uniquely determined by the bottom cell [29]. We remark that the G-4 cell cannot be stacked as such due to the inherent bending deformation.

## 3. Construction of 4-vertex origami structures

In this research, two classes of 4-vertex origami structures will be designed and studied: one is single-layer origami sheets; and the other is origami blocks. This section introduces the construction principles.

### (a) 4-vertex origami sheets

When constructing sheets with 4-vertex cells, to ensure design simplicity and practical feasibility, the component cells are assumed to be of the same type; to ensure geometry compatibility, their length parameters ($a$ and $b$) are set to be identical. However, their sector angles can be different. Hence, we propose two designs: single-component sheets [18] and dual-component sheets.

***Single-component sheets***: Repeating cells of identical geometry in the length and width directions is a straightforward idea to construct sheets without additional geometry constraints, see schematic illustration in figure 2*a*. Waitukaitis et al. have pointed out that such design would introduce three new vertices, namely, the rotated original vertex, the complementary vertex, and the rotated complementary vertex [18]. However, these three vertices remain the same type as the original vertex, and do not change the folding kinematics (unique fold, binding fold, and binding angle) of the original vertex [18]. Hence, only the original vertex needs consideration when studying the single-component sheets. In what follows, this design will be briefly denoted as "(AA)", where the repetitive "A" indicates the construction of sheets with identical cells. Based on this design idea, single-component G-4, GFF, SC, and Miura-ori sheets can be accordingly constructed, and are named as $\text{G-4}_{(\text{AA})}$, $\text{GFF}_{(\text{AA})}$, $\text{SC}_{(\text{AA})}$, and $\text{Miura}_{(\text{AA})}$ sheets, respectively.

***Dual-component sheets*:** Two cells of the same type but with different sector-angle assignments can also be connected under some geometry constraints. A schematic illustration of this design idea is shown in figure 2*b*, where each column is composed of identical cells (A or B), while each row is made up of cells with two different sector-angle assignments (A and B). Such

design is denoted by "(A,B)" for simplicity, where "A" and "B" indicate the two different cells. Based on this design idea, dual-component G-4, GFF, SC, and Miura-ori sheets can be constructed, and are named as $\text{G-4}_{(\text{A, B})}$, $\text{GFF}_{(\text{A, B})}$, $\text{SC}_{(\text{A, B})}$, and $\text{Miura}_{(\text{A, B})}$ sheets, respectively.

Certain geometry constraints must be satisfied by cells A and B so as to have geometry compatible connections. To derive these constraints, an (A-B-A) element is considered so that both A-B and B-A connections are included (figure 2*b*). Cells A and B are characterized by sector angles $\alpha_{Ai}$ and $\alpha_{Bi}$ $(i=1,2,3,4)$, respectively; and their folding status are described by dihedral angles $\rho_{Ai}$ and $\rho_{Bi}$ $(i=1,2,3,4)$, respectively. At the connection between cells A and B, a new 4-vertex cell C is generated, with four sector angles denoted by $\beta_i$ and four folds denoted by $\sigma_i$; at the connection between cells B and A, a new 4-vertex cell D is generated, with four sector angles denoted by $\gamma_i$ and four folds denoted by $\delta_i$. Since each facet is a parallelogram, the sector angles $\beta_i$ and $\gamma_i$ in cells C and D are not independent and can be expressed by $\alpha_{Ai}$ and $\alpha_{Bi}$

$$\begin{aligned}&\beta_1=\pi-\alpha_{B4},\ \beta_2=\pi-\alpha_{B3},\ \beta_3=\pi-\alpha_{A2},\ \beta_4=\pi-\alpha_{A1};\\&\gamma_1=\pi-\alpha_{A4},\ \ \gamma_2=\pi-\alpha_{A3},\ \gamma_3=\pi-\alpha_{B2},\ \gamma_4=\pi-\alpha_{B1}.\end{aligned}\tag{3.1}$$

To ensure the sheet's developability, $\beta_i$ and $\gamma_i$ have to satisfy the constraints $\sum_i \beta_i = 2\pi$ and $\sum_i \gamma_i = 2\pi$, which give rise to

$$\alpha_{A1}+\alpha_{A2}+\alpha_{B3}+\alpha_{B4}=2\pi.\tag{3.2}$$

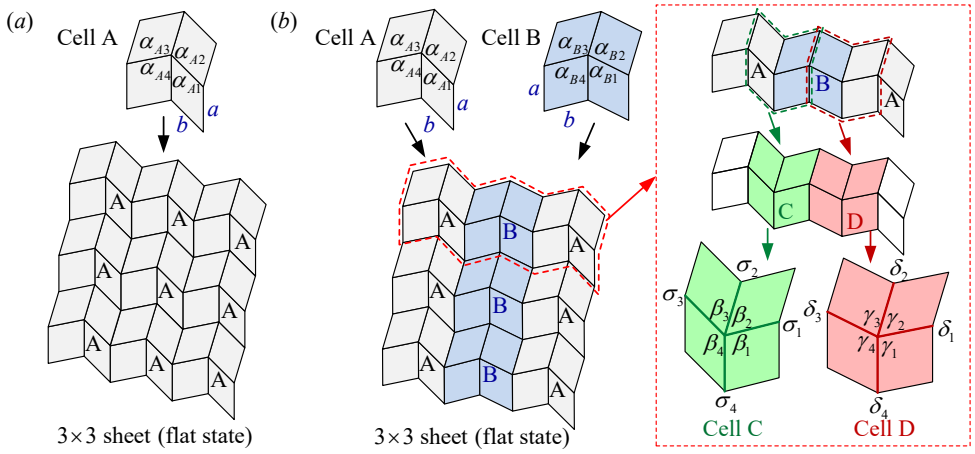


**Figure 2.** Schematic illustrations of the two sheet designs. (*a*) Single-component sheets (AA). (*b*) Dual-component sheets (A, B).

**Table 2**. Geometry constraints and independent sector angles for constructing dual-component sheets (A, B).

| Type | Single cell constraints other than $\sum\alpha_i = 2\pi$ and $\alpha_j < \sum\alpha_{i\neq j}$ | Connecting constraints | Extra constraints to generate cells C and D | Cell C | Cell D | Independent sector angles | |
|---|---|---|---|---|---|---|---|
| | | | | | | # | List |
| G-4$_{(A,B)}$ | / | (3.2) | / | G-4 | G-4 | 5 (A:3; B:2) | $\alpha_{A1},\alpha_{A2},\alpha_{A4};\ \alpha_{B1},\alpha_{B4}$ |
| | | | $\alpha_{B4}=\pi-\alpha_{A2}$ | GFF | G-4 | 4 (A:3; B:1) | $\alpha_{A1},\alpha_{A2},\alpha_{A4};\ \alpha_{B1}$ |
| | | | $\alpha_{B1}=\pi-\alpha_{A3}$ | G-4 | GFF | 4 (A:3; B:1) | $\alpha_{A1},\alpha_{A2},\alpha_{A4};\ \alpha_{B4}$ |
| | | | $\alpha_{B4}=\pi-\alpha_{A2}$, $\alpha_{B1}=\pi-\alpha_{A3}$ | GFF | GFF | 3 (A:3; B:0) | $\alpha_{A1},\alpha_{A2},\alpha_{A4}$ |
| GFF$_{(A,B)}$ | $\alpha_{A1}+\alpha_{A3}=\alpha_{A2}+\alpha_{A4}$, $\alpha_{B1}+\alpha_{B3}=\alpha_{B2}+\alpha_{B4}$ | (3.2) | / | G-4 | G-4 | 3 (A:2; B:1) | $\alpha_{A1},\alpha_{A4};\ \alpha_{B1}$ |
| SC$_{(A,B)}$ | $\alpha_{A1}+\alpha_{A2}=\alpha_{A3}+\alpha_{A4}$, $\alpha_{B1}+\alpha_{B2}=\alpha_{B3}+\alpha_{B4}$ | (3.2) | / | SC | SC | 4 (A:2; B:2) | $\alpha_{A1},\alpha_{A4};\ \alpha_{B1},\alpha_{B4}$ |
| | | | $\alpha_{B4}=\alpha_{A1}$ | Miura-ori | SC | 3 (A:2; B:1) | $\alpha_{A1},\alpha_{A4};\ \alpha_{B1}$ |
| | | | $\alpha_{B1}=\alpha_{A4}$ | SC | Miura-ori | 3 (A:2; B:1) | $\alpha_{A1},\alpha_{A4};\ \alpha_{B4}$ |
| | | | $\alpha_{B4}=\alpha_{A1}$, $\alpha_{B1}=\alpha_{A4}$ | Miura-ori | Miura-ori | 2 (A:2; B:0) | $\alpha_{A1},\alpha_{A4}$ |
| Miura$_{(A,B)}$ | $\alpha_{A1}+\alpha_{A3}=\alpha_{A2}+\alpha_{A4}$, $\alpha_{B1}+\alpha_{B3}=\alpha_{B2}+\alpha_{B4}$; $\alpha_{A1}+\alpha_{A2}=\alpha_{A3}+\alpha_{A4}$, $\alpha_{B1}+\alpha_{B2}=\alpha_{B3}+\alpha_{B4}$ | (3.2) | / | SC | SC | 2 (A:1; B:1) | $\alpha_{A1};\ \alpha_{B1}$ |

Equation (3.2) and the constraints on single cells A and B together constitute the conditions that $\alpha_{Ai}$ and $\alpha_{Bi}$ have to satisfy (Table 2, columns 2 and 3). Moreover, if imposing extra constraints (Table 2, column 4) the newly generated cells C and D can be of different types as cells A and B. Here we assume that the folding directions of the constituent cells in the sheet are identical, i.e., in each cell (A, B, C, and D) it is always fold 2 or 4 (dihedral angles with subscript 2 or 4) that acts as the unique fold, and fold 1 or 3 (dihedral angles with subscript 1 or 3) that acts as the binding fold. It follows that connecting two different G-4 cells together, the middle cells (C and D) can be either G-4 or GFF; connecting two different SC cells together, the middle cells can be either SC or Miura-ori; however, connecting two different GFF cells together, the middle cells can only be G-4; and connecting two different Miura-ori cells together, the middle cells can only be SC. In sum, there are totally ten different cases of dual-component sheets. For each case, the number of independent sector angles and a choice of independent sector angles are listed in table 2, columns 7 and 8.

We remark that such design would also introduce complementary vertices of the A, B, C, and D [18]. However, they will not affect the folding kinematics of the original vertices, and as a result do not need additional consideration.

**(b) 4-vertex origami blocks**

Similar as the sheet construction, stacked units of the same type can be repeated in a plane. Moreover, they can be further stacked along the height direction into a block. To ensure kinematical compatibility, the length parameters at the connecting creases are set to be the same; however, their sector angles can be different. Hence, corresponding to the two sheet designs, two block designs are proposed: single-component blocks and dual-component blocks.

***Single-component blocks*:** Repeating identical stacked units $\mathrm{S_A}$ in three directions can generate a single-component block. Figure 3*a* schematically illustrates this design $(\mathrm{S_A S_A})$, where the nested-in configuration is taken as an example. Based on this design idea, single-component GFF, SC, and Miura-ori blocks can be constructed and are named as $\mathrm{GFF_{S_A S_A}}$, $\mathrm{SC_{S_A S_A}}$, and $\mathrm{Miura_{S_A S_A}}$, respectively.

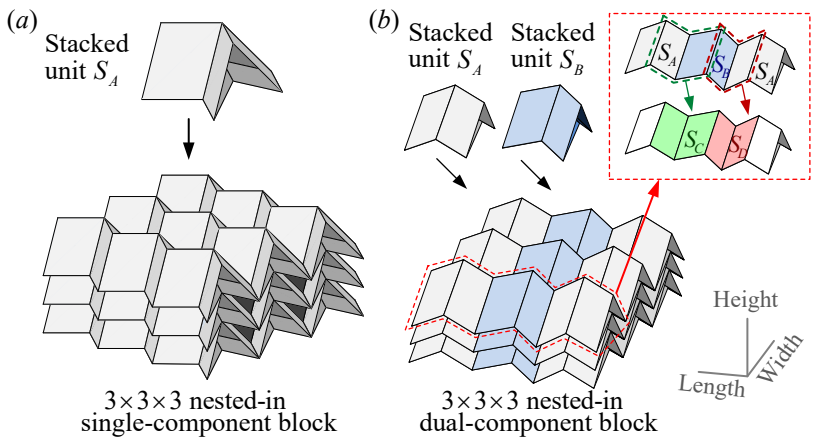


**Figure 3.** Schematic illustration of the two block designs. (*a*) Single-component block $(S_A S_A)$. (*b*) Dual-component block $(S_A, S_B)$.

***Dual-component blocks*:** Stacked units with different sector-angle assignments can also be connected under some geometry constraints. Noting that connecting two different GFF cells will generate an un-stackable G-4 cell at the connection, GFF stacked unit is ruled out for building dual-component blocks, and only SC and Miura-ori cells are considered. Figure 3*b* schematically illustrate this design idea (taking the nested-in configuration as an example), where each column is composed of identical stacked units ($S_A$ or $S_B$), while each row consists of stacked units with two different sector-angle assignments ($S_A$ and $S_B$). The arrangement of stacked units remains the same on each layer of the block. Such design is denoted by "$(S_A, S_B)$", where "$S_A$" and "$S_B$" indicate the two stacked units with different geometries. Based on this design idea, dual-component SC and Miura-ori blocks can be constructed and are named as $SC_{(S_A, S_B)}$ and $Miura_{(S_A, S_B)}$ blocks, respectively.

Similar as the sheet construction, new types of stacked units can be generated at the connection between $S_A$ and $S_B$. Connecting two SC stacked units can generate a SC or Miura-ori stacked unit at the connection; connecting two Miura-ori stacked units, the middle stacked unit can only be SC. For each case, the constraints on the bottom cell geometries are the same as those for constructing dual-component sheets (see table 2). In addition, the stacked units $S_A$ and $S_B$ have to meet an additional constraint to ensure compatible connection

$$\frac{\cos\alpha_{A1}^{I}}{\cos\alpha_{A1}^{II}} = \frac{\cos\alpha_{B1}^{I}}{\cos\alpha_{B1}^{II}}. \tag{3.3}$$

**Table 3**. Geometry constraints and independent sector angles for constructing dual-component blocks $(S_A, S_B)$.

| Type | Constraints on bottom cells | Stacking and connecting constraint | Stacked unit C type | Stacked unit D type | Independent sector angles | |
|---|---|---|---|---|---|---|
| | | | | | # | List |
| $SC_{(S_A, S_B)}$ | Table 2 | (2.2), (3.3) | SC | SC | 5 ($S_A$:3; $S_B$:2) | $\alpha^I_{A1}, \alpha^I_{A4}, \alpha^{II}_{A1}$; $\alpha^I_{B1}, \alpha^I_{B4}$ |
| | | | Miura-ori | SC | 4 ($S_A$:3; $S_B$:1) | $\alpha^I_{A1}, \alpha^I_{A4}, \alpha^{II}_{A1}$; $\alpha^I_{B1}$ |
| | | | SC | Miura-ori | 4 ($S_A$:3; $S_B$:1) | $\alpha^I_{A1}, \alpha^I_{A4}, \alpha^{II}_{A1}$; $\alpha^I_{B4}$ |
| | | | Miura-ori | Miura-ori | 3 ($S_A$:3; $S_B$:0) | $\alpha^I_{A1}, \alpha^I_{A4}, \alpha^{II}_{A1}$ |
| $Miura_{(S_A, S_B)}$ | Table 2 | (2.2) , (3.3) | SC | SC | 3 ($S_A$:2; $S_B$:1) | $\alpha^I_{A1}, \alpha^{II}_{A1}$; $\alpha^I_{B4}$ |

It indicates that the sector angle $\alpha^{II}_{B1}$ of the top cell in $S_B$ are no longer independent, but rather constrained by $S_A$. As a summary, table 3 lists the geometry constraints, the number of independent sector angles, and a choice of independent sector angles for dual-component block construction.

## 4. Principles of achieving self-locking

In this section, we present the principles of achieving self-locking in 4-vertex sheets and blocks. To understand and harness the self-locking property, it is necessary to determine the locations where facet-binding will happen, i.e., to identify the global binding fold during folding; this constitutes the major focus of this section.

### (a) Self-locking mechanisms

Our recent studies have shown that the G-4 and SC cells, the GFF and SC stacked units possess self-locking ability. Two mechanisms contributed to their self-locking behavior have been identified: in-cell facet-binding and inter-cell facet-binding [29]. The first mechanism refers that two facets in the same cell bind together to prevent the cell from further folding; and the latter one indicates that facets of different cells bind together to prevent the structure from further binding.

Hence, self-locking structures can be identified by evaluating whether a 4-vertex structure possess a cell (or stacked unit) with self-locking ability. If a sheet contains a G-4 or SC cell, it will self-lock at a non-flat position. Based on this, self-locking sheets can be identified and are

**Table 4**. Identification of self-locking 4-vertex sheets and blocks.

| Sheet type | | Self-locking | Block type | | Self-locking |
|---|---|---|---|---|---|
| Single-component sheet | $G\text{-}4_{(AA)}$ | • | Single-component block | | |
| | $GFF_{(AA)}$ | | | $GFF_{(S_AS_A)}$ | • |
| | $SC_{(AA)}$ | • | | $SC_{(S_AS_A)}$ | • |
| | $Miura_{(A,B)}$ | | | $Miura_{(S_AS_A)}$ | |
| Dual-component sheet | $G\text{-}4_{(A,B)}$ | • | Dual-component block | | |
| | $GFF_{(A,B)}$ | • | | | |
| | $SC_{(A,B)}$ | • | | $SC_{(S_A,S_B)}$ | • |
| | $Miura_{(A,B)}$ | • | | $Miura_{(S_A,S_B)}$ | • |

summarized in table 4. It reveals that the single-component G-4 and SC sheets and all of the due-component sheets possess self-locking ability. Similarly, based on whether containing a GFF or SC stacked units, self-locking blocks can be identified and are summarized in table 4. It shows that single-component GFF and SC blocks and all of the dual-component blocks possess self-locking ability.

**(b) Self-locking in 4-vertex sheets**

This subsection aims at determining the global binding folds of the 4-vertex sheets. To facilitate the analysis, we still assume that fold 1 in cell A is capable of fully closing to zero (i.e., $\rho_1$ in single-component design or $\rho_{A1}$ in dual-component design is the binding fold). Hence, in single-component G-4 and SC sheets ($G\text{-}4_{(AA)}$ and $SC_{(AA)}$), facets astride the binding fold (i.e., $\rho_1$) in each component cell will always bind first, inducing self-locking of the whole sheet [29]. Figure 4*a* and 4*b* show the fully folded state of a $G\text{-}4_{(AA)}$ and $SC_{(AA)}$ sheet, respectively, where the closing folds are denoted by bold lines, and the binding facets are denoted by shades.

In dual-component sheets, dihedral angles of cells A, B, C, and D in the sheet can be determined and expressed as functions of $\rho_{A1}$ by successively employing the spherical trigonometry, see illustration in figure 5. Hence, folding is still a one degree-of-freedom motion. Note that some folds are shared by two cells, which gives rise to identity relations $\rho_{A1}=\sigma_3$, $\rho_{B3}=\sigma_1$, $\rho_{B1}=\delta_3$, and $\rho_{A3}=\delta_1$.

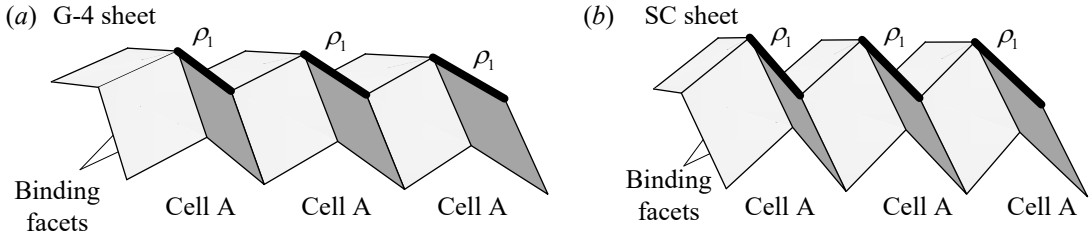


**Figure 4.** Single-component self-locking sheets at the fully-folded state. (*a*) 3×1 G-4 sheet ($\alpha_1 = 36^\circ$, [illegible], $\alpha_4 = 72^\circ$) and (*b*) 3×1 SC sheet ($\alpha_1 = 36^\circ$, [illegible]). The binding facets (shade) and the binding folds (bold) are pointed out.

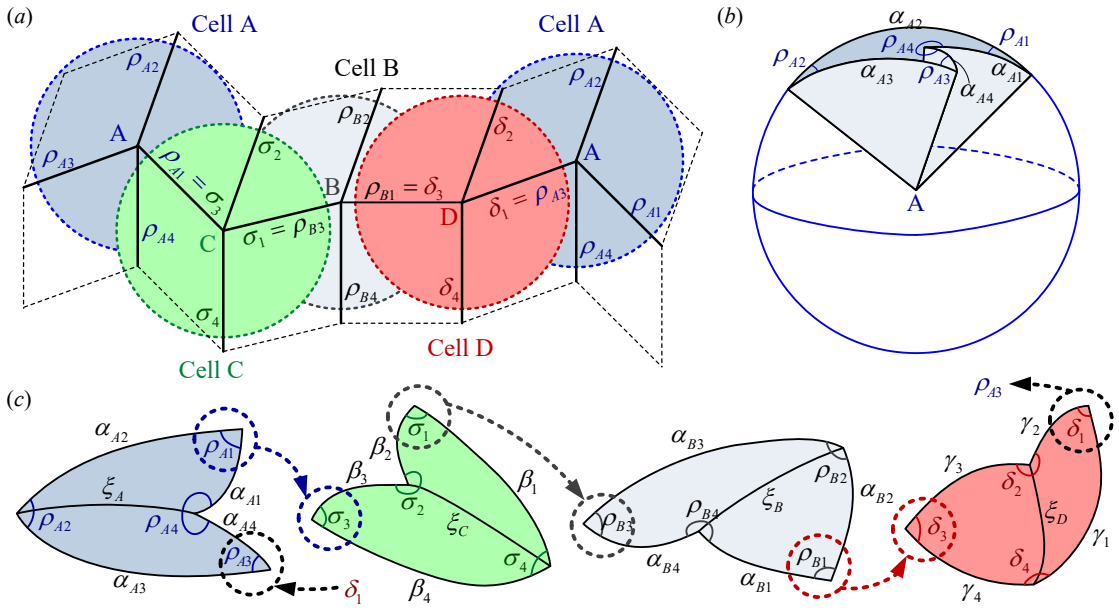


**Figure 5.** Spherical geometry of the dual-component sheets. (*a*) Illustration of the flat sheet geometry, where each 4-vertex is denoted by a unit circle with center A, B, C, and D, corresponding to cells A, B, C, and D (dashed), respectively. (*b*) Illustration of the partially-folded 4-vertex A. The outer edges of the 4-vertex locates on a unit sphere, and cut the sphere surface into a spherical polygons. (*c*) Schematic plots of the spherical polygons generated by cutting the sphere surfaces with the 4-vertices. The spherical polygons from left to right correspond to vertices A, C, B, and D, respectively. In each spherical polygon, $\xi$ divides it into two spherical triangles, and all the dihedral angles can hence be calculated based on spherical trigonometry. The shared dihedral angles in different polygons are denoted by dashed circles.

Once having all the dihedral angles of cells A, B, C, and D, the problem of determining the global binding fold is reduced to examining which dihedral angle first reaches zero. This dihedral angle can only stay at one of the possible binding fold in each cell, i.e., $\rho_{A1}$ and $\rho_{A3}$ in cell A (equivalently, $\sigma_3$ in cell C and $\delta_1$ in cell D), $\rho_{B1}$ and $\rho_{B3}$ in cell B (equivalently, $\delta_3$ in cell D and $\sigma_1$ in cell C). Using the assumption that $\rho_{A1}$ is the binding folding of cell A (hence,

$\rho_{A1} < \rho_{A3}$), we are able to determine the global binding fold of the sheet by comparing the three dihedral angles $\rho_{A1}$, $\rho_{B1}$, and $\rho_{B3}$, i.e.,

$$\text{Binding fold}=\min\{\rho_{A1},\rho_{B1},\rho_{B3}\}, \tag{4.1}$$

where the dihedral angles $\rho_{B1}$ and $\rho_{B2}$ can be written as functions of $\rho_{A1}$

$$\begin{aligned}\rho_{B1} &= \arccos\left(\frac{\sin\alpha_{A1}\sin\alpha_{A2}\cos\rho_{A1}+\cos\alpha_{A1}\cos\alpha_{A2}-\cos\alpha_{B1}\cos\alpha_{B2}}{\sin\alpha_{B1}\sin\alpha_{B2}}\right),\\ \rho_{B3} &= \arccos\left(\frac{\sin\alpha_{A1}\sin\alpha_{A2}\cos\rho_{A1}+\cos\alpha_{A1}\cos\alpha_{A2}-\cos\alpha_{B3}\cos\alpha_{B4}}{\sin\alpha_{B3}\sin\alpha_{B4}}\right).\end{aligned} \tag{4.2}$$

In what follows, explicit conditions for determining the global biding fold will be derived for each case. Notations "$\mathrm{XX_A}+\mathrm{XX_B}\rightarrow\mathrm{XX_C}+\mathrm{XX_D}$" are used to indicate the types of the component cells and the newly-generated cells in a sheet.

We first study the most generic case $\text{G-4}_\text{A}+\text{G-4}_\text{B}\rightarrow\text{G-4}_\text{C}+\text{G-4}_\text{D}$. Here, the sector angles $\alpha_{A1},\alpha_{A2},\alpha_{A4}$ in cell A and $\alpha_{B1},\alpha_{B4}$ in cell B are independent. According to table 2, the sector angles $\alpha_{B2}$ and $\alpha_{B3}$ in equation (4.2) can be written as $\alpha_{B2}=\alpha_{A1}+\alpha_{A2}-\alpha_{B1}$, $\alpha_{B3}=2\pi-(\alpha_{A1}+\alpha_{A2}+\alpha_{B4})$. Through algebraic analysis, condition (4.1) can be rewritten as

$$\text{Binding fold}=\begin{cases}\rho_{A1}, & \text{if } \cos(\alpha_{A1}-\alpha_{A2})<\cos(2\alpha_{B1}-\alpha_{A1}-\alpha_{A2})\\ & \&\ \cos(\alpha_{A1}-\alpha_{A2})<\cos(\alpha_{A1}+\alpha_{A2}+2\alpha_{B4});\\ \rho_{B1}, & \text{if } \cos(\alpha_{A1}-\alpha_{A2})>\cos(2\alpha_{B1}-\alpha_{A1}-\alpha_{A2})\\ & \&\ \cos(2\alpha_{B1}-\alpha_{A1}-\alpha_{A2})<\cos(\alpha_{A1}+\alpha_{A2}+2\alpha_{B4});\\ \rho_{B3}, & \text{if } \cos(\alpha_{A1}-\alpha_{A2})>\cos(\alpha_{A1}+\alpha_{A2}+2\alpha_{B4})\\ & \&\ \cos(2\alpha_{B1}-\alpha_{A1}-\alpha_{A2})>\cos(\alpha_{A1}+\alpha_{A2}+2\alpha_{B4}).\end{cases} \tag{4.3}$$

Due to the generality of this case, the obtained condition (4.3) applies to all the other cases. Moreover, by incorporating extra constraints on sector angles (listed in table 2) and the identity relations among dihedral angles, simplified conditions can be derived.

Table 5 lists the conditions and the global binding folds, for each case of the dual-component sheets. Detailed expressions of the conditions are provided in Electronic Supplementary Material (ESM). For each type of the dual-component sheet, an example is sketched in figure 6.

**Table 5**. Locking behavior of the self-locking sheets.

| Sheet types | Condition | Global binding folds | Flat-folded locking plane | Schematic illustrations |
|---|---|---|---|---|
| $G\text{-}4_A+G\text{-}4_B \rightarrow G\text{-}4_C+G\text{-}4_D$ | (4.3) | $\rho_{A1}$ | / | |
| | | $\rho_{B1}$ | / | figure 6*a* |
| | | $\rho_{B3}$ | / | |
| $G\text{-}4_A+G\text{-}4_B \rightarrow GFF_C+G\text{-}4_D$ | ESM (A 1) | $\rho_{A1}$, $\rho_{B3}$ | C | figure 6*b* |
| | | $\rho_{B1}$ | / | |
| $G\text{-}4_A+G\text{-}4_B \rightarrow G\text{-}4_C+GFF_D$ | ESM (A 2) | $\rho_{A1}$ | / | |
| | | $\rho_{B3}$ | / | figure 6*c* |
| $G\text{-}4_A+G\text{-}4_B \rightarrow GFF_C+GFF_D$ | ESM (A 3) | $\rho_{A1}$, $\rho_{B3}$ | C | figure 6*d* |
| $GFF_A+GFF_B \rightarrow G\text{-}4_C+G\text{-}4_D$ | ESM (A 4) | $\rho_{A1}$, $\rho_{A3}$ | A | |
| | | $\rho_{B1}$, $\rho_{B3}$ | B | figure 6*e* |
| $SC_A+SC_B \rightarrow SC_C+SC_D$ | ESM (A 6) | $\rho_{A1}$ | / | |
| | | $\rho_{B1}$ | / | figure 6*f* |
| | | $\rho_{B3}$ | / | |
| $SC_A+SC_B \rightarrow Miura_C+SC_D$ | ESM (A 7) | $\rho_{A1}$, $\rho_{B3}$ | C | figure 6*g* |
| | | $\rho_{B1}$ | / | |
| $SC_A+SC_B \rightarrow SC_C+Miura_D$ | ESM (A 8) | $\rho_{A1}$ | / | |
| | | $\rho_{B3}$ | / | figure 6*h* |
| $SC_A+SC_B \rightarrow Miura_C+Miura_D$ | ESM (A 9) | $\rho_{A1}$, $\rho_{B3}$ | C | figure 6*i* |
| $Miura_A+Miura_B \rightarrow SC_C+SC_D$ | ESM (A 10) | $\rho_{A1}$, $\rho_{A3}$ | A | |
| | | $\rho_{B1}$, $\rho_{B3}$ | B | figure 6*j* |

### (c) Self-locking in 4-vertex blocks

Our previous work [29] has determined the binding facets for single-component stacked blocks (GFF and SC). For the sake of completeness, we briefly review the results here. The assumption that $\rho_1^I$ is the binding fold of the bottom cell will be employed. Figure 7*a* and 7*b* show the fully folded states of a GFF block and a SC block, respectively, with both the nested-in and bulged-out configurations. For the GFF stacked block, at the nested-in configuration, facets of the bottom cell and facets of the top cell will bind together (i.e., inter-cell facet-binding), and the connecting crease between them ($\rho_C$) act as the global binding folds; at the bulged-out configuration, the bottom cell folds flat (i.e., in-cell facet-binding). For the SC stacked block, at the nested in configuration, two facets of the bottom cell and two facets of the top cell bind together

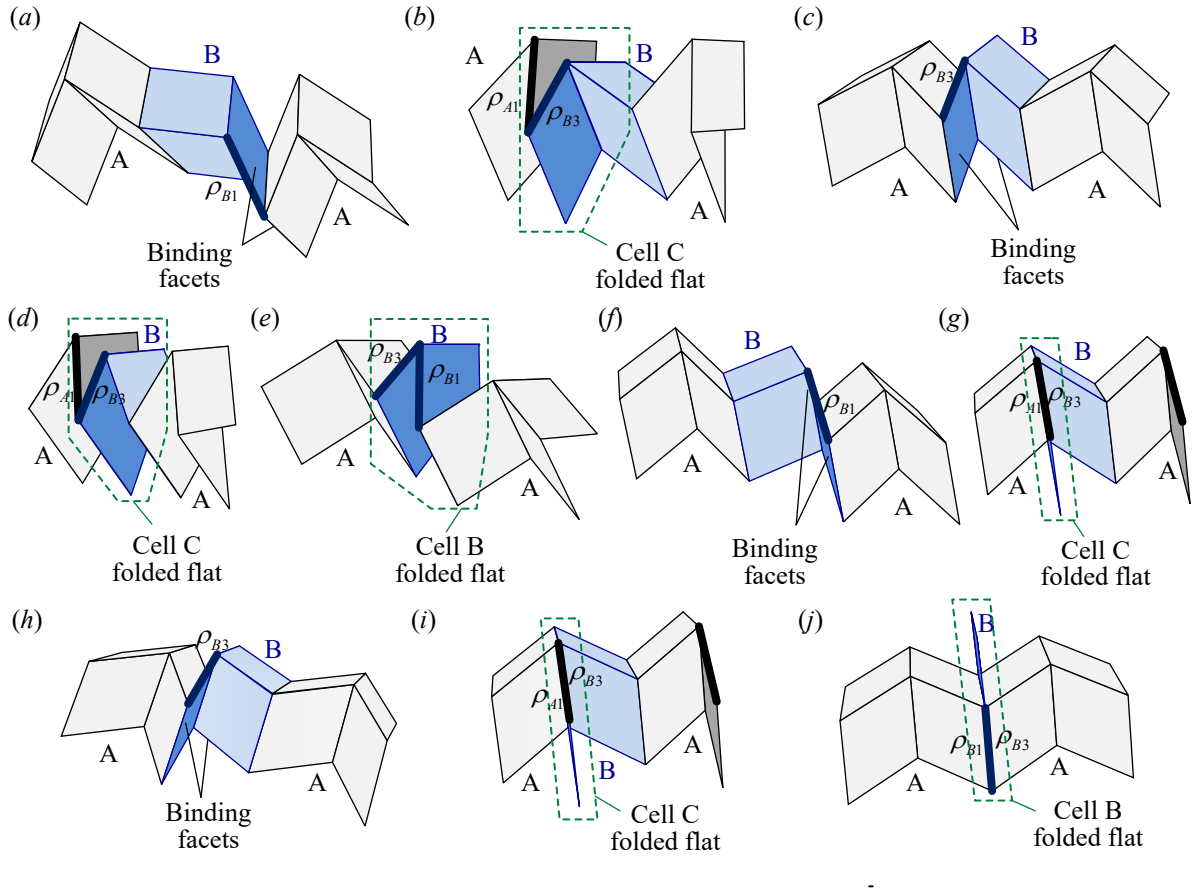


**Figure 6.** Dual-component self-locking sheets at fully folded states, where the binding facets (dark facets), the global binding folds (bold creases), and the flat-folded cells (dashed polygons) are marked. "A" and "B" indicate the component cell A and cell B, respectively.

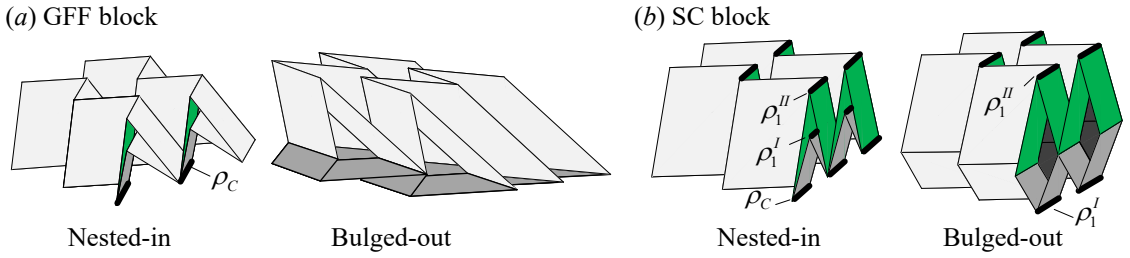


**Figure 7.** Single-component self-locking blocks at the fully-folded state, with both the nested-in and bulged-out configurations. (*a*) $2 \times 2 \times 1$ GFF block ( $\alpha_1^I = 36^\circ, \ldots_4$ $\ldots^\circ, \ldots_1$ $\ldots^\circ$ ) and (*b*) $2 \times 2 \times 1$ SC blocks ( $\alpha_1^I = 36^\circ, \ldots_4$ $\ldots^\circ, \ldots_1$ $\ldots^\circ$ ). The binding facets (shade) and the binding folds (bold) are marked; the binding connecting crease is denoted by $\rho_C$.

simultaneously (i.e., in-cell and inter-cell facet-binding), $\rho_1^I$, $\rho_1^{II}$, and $\rho_C$ act as the binding folds; at the bulged-out configuration, two facets in the bottom cell bind together, and two facets of the top cell bind together at the same time, but they do not inter-bind (i.e., in-cell facet-binding), $\rho_1^I$ and $\rho_1^{II}$ are the binding folds.

In dual-component blocks, self-locking is caused by the facet-binding in SC stacked units. Note that when a SC cell self-locks, the corresponding SC stacked unit self-locks simultaneously, and the binding folds in the bottom and top cells are corresponding to each other. As a result, the conditions for determining the global binding fold in dual-component SC and Miura sheets are still valid for the corresponding stacked blocks. We list these conditions in table 6, where notations "$\mathrm{XX}_{\mathrm{S_A}}+\mathrm{XX}_{\mathrm{S_B}} \rightarrow \mathrm{XX}_{\mathrm{S_C}}+\mathrm{XX}_{\mathrm{S_D}}$" are adopted to indicate the types of component stacked units and the newly generated stacked units in a block. Detailed expressions are provided in the Electronic Supplementary Material (ESM). For each type of the dual-component block, an example is illustrated in figure 8.

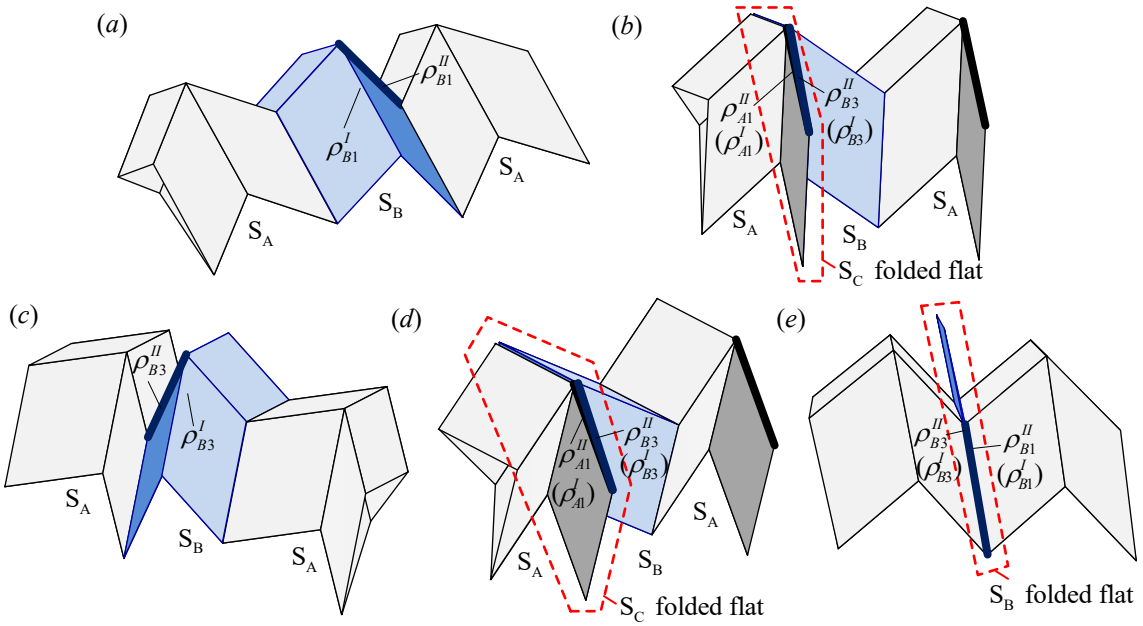


**Figure 8.** Dual-component self-locking blocks at the fully-folded state, with the nested-in configuration as an example. The binding facets (shade), the global binding folds (bold creases), and the flat-folded cells (dashed polygons) are marked. "$\mathrm{S_A}$" and "$\mathrm{S_B}$" indicate the component stacked units.

**Table 6**. Locking behavior of the self-locking blocks.

| Sheet types | Condition | Global binding folds | Flat-folded locking plane | Schematic illustrations |
|---|---|---|---|---|
| $SC_{S_A}+SC_{S_B}\rightarrow SC_{S_C}+SC_{S_D}$ | ESM(B 1) | $\rho^I_{A1},\rho^{II}_{A1}$ | / | |
| | | $\rho^I_{B1},\rho^{II}_{B1}$ | / | figure 8*a* |
| | | $\rho^I_{B3},\rho^{II}_{B3}$ | / | |
| $SC_{S_A}+SC_{S_B}\rightarrow Miura_{S_C}+SC_{S_D}$ | ESM (B 2) | $\rho^I_{A1},\rho^{II}_{A1};\ \rho^I_{B3},\rho^{II}_{B3}$ | $S_C$ | figure 8*b* |
| | | $\rho^I_{B1},\rho^{II}_{B1}$ | / | |
| $SC_{S_A}+SC_{S_B}\rightarrow SC_{S_C}+Miura_{S_D}$ | ESM (B 3) | $\rho^I_{A1},\rho^{II}_{A1}$ | / | |
| | | $\rho^I_{B3},\rho^{II}_{B3}$ | / | figure 8*c* |
| $SC_{S_A}+SC_{S_B}\rightarrow Miura_{S_C}+Miura_{S_D}$ | ESM (B 4) | $\rho^I_{A1},\rho^{II}_{A1};\ \rho^I_{B3},\rho^{II}_{B3}$ | $S_C$ | figure 8*d* |
| $Miura_{S_A}+Miura_{S_B}\rightarrow SC_{S_C}+SC_{S_D}$ | ESM (B 5) | $\rho^I_{A1},\rho^{II}_{A1};\ \rho^I_{A3},\rho^{II}_{A3}$ | $S_A$ | |
| | | $\rho^I_{B1},\rho^{II}_{B1};\ \rho^I_{B3},\rho^{II}_{B3}$ | $S_B$ | figure 8*e* |

### (d) Dual-component tessellation designs

Note that randomly arranging the component cells A and B (or stacked units $S_A$ and $S_B$) in a row will not create new cells other than C and D (or new stacked units other than $S_C$ and $S_D$). Hence, the conditions for determining global binding folds keep valid for any tessellation. Basically, two tessellation designs are possible: (1) an alternate arrangement of cells A and B (or stacked units $S_A$ and $S_B$) to ensure periodicity, see schematic illustration in figure 9*a*; (2) repetition of a component cell (or stacked unit) at certain positions of the structure (figure 9*b*).

We want to remark that theoretically, self-locking structures can be constructed with more than two component cells (or stacked units). If introducing an additional component cell (or stacked unit) with extra geometry constraints, the structure still retains a single degree-of-freedom for folding, and the global binding folds are still consistent with the dihedral angle that first reaches zero. Hence, incorporating more components will not alter or enrich the locking behavior; rather, it will complicate the structure design and manufacturing. This is why only single-component and dual-component structures are considered in this research.

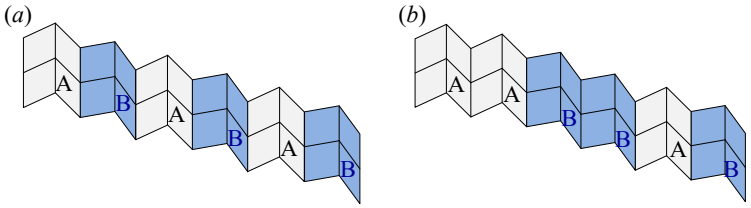


**Figure 9.** Dual-component sheet tessellations. (a) An alternate arrangement of cells A and B. (b) Repetition of cells A and B at certain positions of the structure.

## 5. Programmable flat-folded locking planes and locking points

Locking points indicate the locations where facet-binding happens, i.e., the locations where the global binding folds locate. Particularly, note that in the dual-component structures, flat-foldable cells or stacked units can be included, even though the sheet or block as a whole does not possess flat-foldability. Hence, if the global binding folds locate in the flat-foldable cells or stacked units, a flat-folded locking plane can be generated, which is a particular type of locking point.

The number of locking points and their locations are important information for the utilization of self-locking structures. For example, the facets/creases material at the locking points needs careful selection so as to tailor the structure's mechanical property. Active materials or actuators are always set at the locking points for effective actuation and folding. In this section, we show that with the dual-component designs, the flat-folded locking planes and the locking points are programmable in terms of number and locations.

### (a) Programmable flat-folded locking planes

Based on whether the global binding folds locate in the flat-foldable cells or flat-foldable stacked units, the flat-folded locking planes can be determined and are listed in tables 5 and 6, respectively. Note that such flat-folded locking plane cannot be achieved in single-component designs; it is a new attribute brought by dual-component designs. In addition, by changing the tessellation of component cells (or stacked units), the location and the number of flat-folded locking planes are programmable. Figure 10 displays such an example that by tessellating three Miura-ori cells A and three Miura-ori cells B, we could obtain sheets with one, two, and three flat-folded locking planes. Note that the number of facets that are stacked up at the flat-folded locking planes are designable, which could be exploited for tailoring the structure's stability and loading capacity.

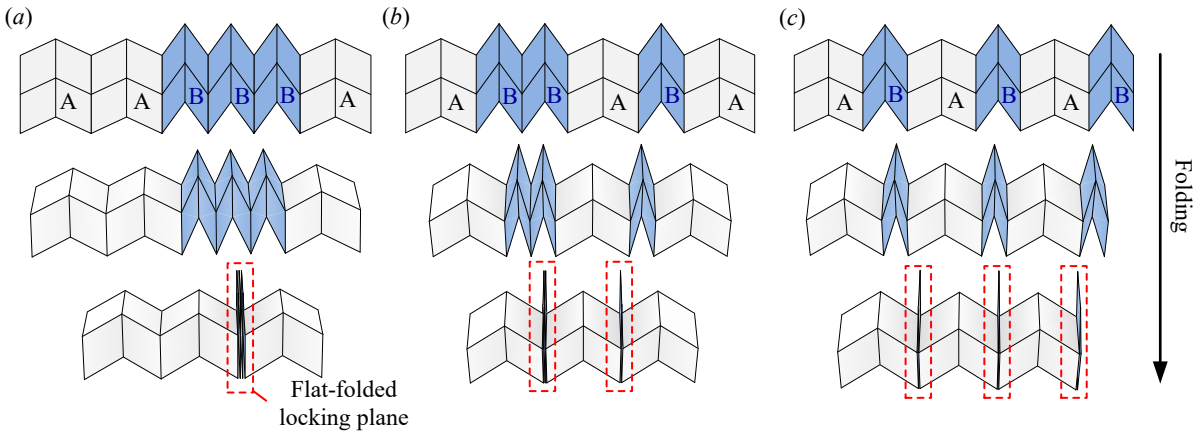


**Figure 10.** Illustration of programmable flat-folded locking planes in self-locking sheets. The sheet in (a), (b), and (c) are made up of three Miura-ori cells A and three Miura-ori cells B, but with different tessellation designs. One, two, and three flat-folded locking planes (dashed rectangles) are generated when the sheets are fully folded.

## (b) Programmable locking points

In a single-component structure, the locking points cannot be programmed; there are always $n$ locking points locating at the binding fold in each component cell (or stacked unit) (figure 11*a*). However, in dual-component structures, we could program the number and location of the locking points by employing different tessellations.

To examine such programmability, we use the sheet as an example for illustration purposes. We assume that a dual-component sheet consists of $n$ component cells, with $n_A$ cells A and $n_B$ cells B ($n_A \geq 1$, $n_B \geq 1$, and $n_A + n_B = n$). If the sheet does not contain any flat-folded locking plane, there would be either $n_A$ or $n_B$ locking points, depending on whether the global binding folds (i.e., the locking points) locate in cells A or cells B (figure 11*b*). If flat-folded locking planes are generated in cells A or cells B, the number of locking points can be varied between 1 and $\min\{n_A, n_B\}$ (or $\min\{n_A, n_B\}+1$, if locking points exist on both ends of the structure). In this specific case, the number of locking points depends on the tessellation of cells A and B: that is, it reaches the minimum when all of the flat-folded cells are concentrated at one position (figure 11*c*), and reaches maximum if every two flat-folded cells are separated by the other type of cell (figure 11*d*). If flat-folded locking planes locate in cells C, both cells A and B have binding facets, and the number of locking points can be varied between $\max\{n_A, n_B\}$ and $n$. The number of locking points again depends on the cell tessellation. The minimum is achieved when the cell arrangement allows as much cells C as possible (figure 11*e*); the

maximum is achieved if cell C is not generated in the sheet (i.e., there is no "A-B" connection in the sheet) (figure 11*f*). The number of locking points for both dual-component sheets and blocks are summarized in table 7.

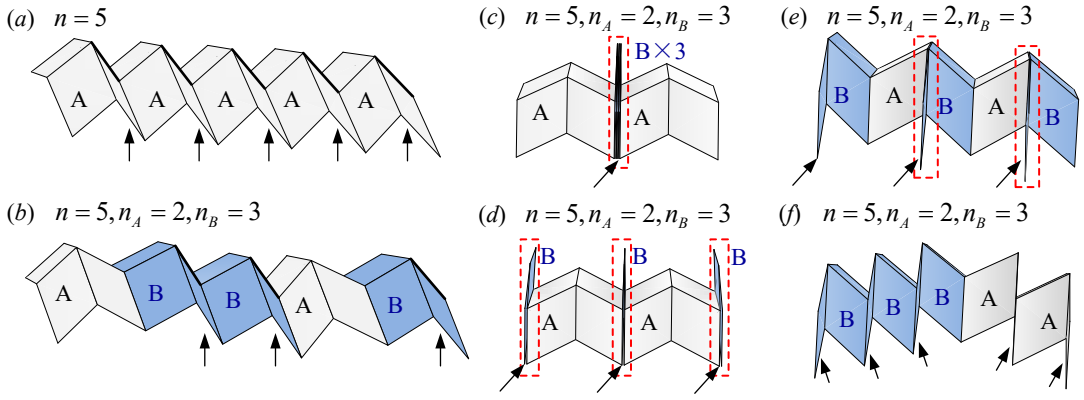


**Figure 11.** Illustration of programmable locking points in self-locking sheets. The locking points are indicated by arrows, and the flat-regions are indicated by dashed rectangles. (*a*) Single-component sheet. (*b*) Dual-component sheet without flat-folded locking plane; it has 3 locking points. (*c*) Dual-component sheet with flat-folded locking planes generated in cells B; it has the minimum number of locking points, 1. (*d*) Dual-component sheet with flat-folded locking plane generated in cells B; it has the maximum number of locking points, 3. (*e*) Dual-component sheet with flat-folded locking plane generated in cells C; it has the minimum number of locking points, 3. (*f*) Dual-component sheet with flat-folded locking plane generated in cells C; it has the maximum number of locking points, 5.

## 6. Programmable deformability

Self-locking provides an origami structure with the ability to reach and maintain a specified configuration. The deformation achieved during the folding process is determined by the origami geometry and the tessellation methods. Here we define the deformation range as

$$\eta = \frac{L_0 - L_f}{L_0}. \tag{6.1}$$

where $L_f$ is the length of the structure when self-locking occurs, and $L_0$ is the initial length when the origami sheet (or the bottom cells of the block) are flat. Hence, $\eta$ measures the deformability of the self-locking structure; the larger the value is, the stronger its deformability.

We still take the sheet as an example to examine how dual-component designs contribute to the structures' deformability. In single-component sheets, it is noticed that the deformation range depends only on the constituent 4-vertex design (say, $\eta_A$). However, in dual-component designs,

**Table 7**. Kinematical properties of self-locking structures.

| | Type | Global binding folds | # of locking points | Deformation range $\eta$ |
|---|---|---|---|---|
| Sheets | $\text{G-4}_{(AA)}$ | $\rho_1$ | $n$ | $\eta_A$ |
| | $\text{SC}_{(AA)}$ | $\rho_1$ | $n$ | $\eta_A$ |
| | $\text{G-4}_A+\text{G-4}_B \rightarrow \text{G-4}_C+\text{G-4}_D$ | $\rho_{A1}$<br>$\rho_{B1}$ or $\rho_{B3}$ | $n_A$<br>$n_B$ | $(\eta_A,\ \eta_B)$ |
| | $\text{G-4}_A+\text{G-4}_B \rightarrow \text{GFF}_C+\text{G-4}_D$ | $\rho_{B1}$<br>$\rho_{A1},\rho_{B3}$ | $n_B$<br>$[\max\{n_A,n_B\},\ n]$ | $(\eta_A,\ \eta_B)$ |
| | $\text{G-4}_A+\text{G-4}_B \rightarrow \text{G-4}_C+\text{GFF}_D$ | $\rho_{A1}$<br>$\rho_{B3}$ | $n_A$<br>$n_B$ | $(\eta_A,\ \eta_B)$ |
| | $\text{G-4}_A+\text{G-4}_B \rightarrow \text{GFF}_C+\text{GFF}_D$ | $\rho_{A1},\rho_{B3}$ | $[\max\{n_A,n_B\},\ n]$ | $(\eta_A,\ \eta_B)$ |
| | $\text{GFF}_A+\text{GFF}_B \rightarrow \text{G-4}_C+\text{G-4}_D$ | $\rho_{A1},\rho_{A3}$ or $\rho_{B1},\rho_{B3}$ | $[1,\ \min\{n_A,n_B\}(+1)]$ | $(\eta_A$ or $\eta_B,\ 1)$ |
| | $\text{SC}_A+\text{SC}_B \rightarrow \text{SC}_C+\text{SC}_D$ | $\rho_{A1}$<br>$\rho_{B1}$ or $\rho_{B3}$ | $n_A$<br>$n_B$ | $(\eta_A,\ \eta_B)$ |
| | $\text{SC}_A+\text{SC}_B \rightarrow \text{Miura}_C+\text{SC}_D$ | $\rho_{B1}$<br>$\rho_{A1},\rho_{B3}$ | $n_B$<br>$[\max\{n_A,n_B\},\ n]$ | $(\eta_A,\ \eta_B)$ |
| | $\text{SC}_A+\text{SC}_B \rightarrow \text{SC}_C+\text{Miura}_D$ | $\rho_{A1}$<br>$\rho_{B3}$ | $n_A$<br>$n_B$ | $(\eta_A,\ \eta_B)$ |
| | $\text{SC}_A+\text{SC}_B \rightarrow \text{Miura}_C+\text{Miura}_D$ | $\rho_{A1},\rho_{B3}$ | $[\max\{n_A,n_B\},\ n]$ | $(\eta_A,\ \eta_B)$ |
| | $\text{Miura}_A+\text{Miura}_B \rightarrow \text{SC}_C+\text{SC}_D$ | $\rho_{A1},\rho_{A3}$ or $\rho_{B1},\rho_{B3}$ | $[1,\ \min\{n_A,n_B\}(+1)]$ | $(\eta_A$ or $\eta_B,\ 1)$ |
| Blocks | $\text{GFF}_{(S_A S_A)}$ | $\rho_C$ or $\rho_1^I,\rho_3^I$ | $n$ | $\eta_A$ |
| | $\text{SC}_{(S_A S_A)}$ | $\rho_C,\ \rho_1^I,\rho_1^{II}$ | $n$ | $\eta_A$ |
| | $\text{SC}_{S_A}+\text{SC}_{S_B} \rightarrow \text{SC}_{S_C}+\text{SC}_{S_D}$ | $\rho_{A1}^I,\rho_{A1}^{II}$<br>$\rho_{B1}^I,\rho_{B1}^{II}$ or $\rho_{B3}^I,\rho_{B3}^{II}$ | $n_A$<br>$n_B$ | $(\eta_A,\ \eta_B)$ |
| | $\text{SC}_{S_A}+\text{SC}_{S_B} \rightarrow \text{Miura}_{S_C}+\text{SC}_{S_D}$ | $\rho_{B1}^I,\rho_{B1}^{II}$<br>$\rho_{A1}^I,\rho_{A1}^{II};\ \rho_{B3}^I,\rho_{B3}^{II}$ | $n_B$<br>$[\max\{n_A,n_B\},\ n]$ | $(\eta_A,\ \eta_B)$ |
| | $\text{SC}_{S_A}+\text{SC}_{S_B} \rightarrow \text{SC}_{S_C}+\text{Miura}_{S_D}$ | $\rho_{A1}^I,\rho_{A1}^{II}$<br>$\rho_{B3}^I,\rho_{B3}^{II}$ | $n_A$<br>$n_B$ | $(\eta_A,\ \eta_B)$ |
| | $\text{SC}_{S_A}+\text{SC}_{S_B} \rightarrow \text{Miura}_{S_C}+\text{Miura}_{S_D}$ | $\rho_{A1}^I,\rho_{A1}^{II};\ \rho_{B3}^I,\rho_{B3}^{II}$ | $[\max\{n_A,n_B\},\ n]$ | $(\eta_A,\ \eta_B)$ |
| | $\text{Miura}_{S_A}+\text{Miura}_{S_B} \rightarrow \text{SC}_{S_C}+\text{SC}_{S_D}$ | $\rho_{A1}^I,\rho_{A1}^{II};\ \rho_{A3}^I,\rho_{A3}^{II}$<br>or $\rho_{B1}^I,\rho_{B1}^{II};\ \rho_{B3}^I,\rho_{B3}^{II}$ | $[1,\ \min\{n_A,n_B\}(+1)]$ | $(\eta_A$ or $\eta_B,\ 1)$ |

other than tailoring the constituent cell designs, the structure's deformability can also be programmed by adjusting the composition proportion of cells A and B. To illustrate such

programmability, we assume that when the sheet is fully folded, cell A contracts from initial length $l_{A0}$ to $l_{Af}$, with deformation rage $\eta_A = (l_{A0} - l_{Af})/l_{A0}$; and cell B contracts from the initial length $l_{B0}$ to $l_{Bf}$, with deformation range $\eta_B = (l_{B0} - l_{Bf})/l_{B0}$. Note that $l_{Af}$ and $l_{Bf}$ may not necessarily be the minimum length associated to their individual locking configurations. Hence, the initial and final lengths of the structure can be written as

$$\begin{aligned} L_0 &= n_A l_{A0} + n_B l_{B0}, \\ L_f &= n_A l_{Af} + n_B l_{Bf}. \end{aligned} \tag{6.2}$$

Taking $n_A$, $n_B$, $l_{A0}$, $l_{B0}$, $\eta_A$, and $\eta_B$ as the independent variables, the deformation range of the sheet $\eta$ yields

$$\eta = \frac{n_A \eta_A l_{A0} + n_B \eta_B l_{B0}}{n_A l_{A0} + n_B l_{B0}}. \tag{6.3}$$

Note that with fixed cell designs and fixed numbers of cells A and B, the structure's deformability does not depend on cell tessellations.

The extreme values of $\eta$ can be obtained by considering two limiting cases and assuming that there are infinity number of cells. In the first case, there is only one cell B, i.e., $n_A \to (n-1)$ and $n_B \to 1$, we have $\tilde{\imath}$ in the second case, there is only one cell A, i.e., $n_A \to 1$, $n_B \to n-1$, we have $\tilde{\imath}$ Hence, by changing the tessellation based on requirements, the deformation range $\eta$ can take any value between $\eta_{\mathrm{A}}$ and $\eta_B$. Particularly, if cell A or B is flat-foldable (i.e., $\eta_{\mathrm{A}} \to 1$ or $\eta_B \to 1$), $\eta \to 1$ becomes possible, indicating that the sheet would possess strong deformability (close to flat-foldability) as well as self-locking ability. Deformation range of the stacked blocks can be similarly analyzed, summarized in table 7.

## 7. Locking-induced stiffness jump

In addition to the kinematic properties, this section explores the change in stiffness property due to self-locking. Before facet-binding occurs, the origami structure deforms following the kinematic relationships of rigid-folding: that is, the crease materials are bent like flexible hinges but the facet materials remain un-deformed. Hence, the overall structure tangent stiffness comes from the bending stiffness of the crease line material [15,18,31,32]. After self-locking, the structure cannot be rigidly folded any more, and further loading will instead directly deform the facet materials. Since the facet is typically stiffer than the crease, the overall stiffness can

become significantly higher. Since the kinematic relationship of rigid-folding is no longer valid, estimating the increased stiffness after self-locking would require finite element analyses [33] or experiments [34]. In this research, we experimentally demonstrate the locking-induced stiffness change based on two SC stacked unit prototypes.

Two SC stacked unit prototypes are fabricated as follows. The origami facets are water jet cut out of steel plates (with thickness 0.254 *mm*), and the creases are made of adhesive-back polyethylene films (with thickness 0.127 *mm*). Hence, the creases material is much softer than the facets. Pre-folded spring-steel stripes are applied to crease lines to generate some bending stiffness. The two stacked units are of the same geometry but with different bending stiffness at the creases (i.e., pasting spring-steel stripes with different thickness; unit 1: 0.10 *mm*, unit 2: 0.18 *mm*).

We take eight compression tests in the length direction on each stacked unit separately. Figure 12*a* shows the force-displacement curves together with the standard deviations (shades). It shows that each curve consists of two segments with significantly different slopes. Linear regression is performed on the first two curve segments, which gives the corresponding approximated structure stiffness, shown in figure 12*b*. For both units, the overall stiffness experiences a sharp jump from low values (0.341 and 0.877 *N/mm*) to high values (38.7 and 104.6 *N/mm*) due to self-locking. Before self-locking happens, the stiffness mainly comes from the pre-bended spring-steel stripes at the creases; after the self-locking point, the facet material bending contribute to the stiffness upsurge. Note that the compression tests are limited within a safety range to prevent the prototypes from being damaged. Figure 12*c* displays the photos of the stacked unit at three states: the initial stress-free state (*i*), the self-locking instant (*ii*), and a state after self-locking, with facet-bending (*iii*).

Figure 12 reveals an interesting locking-induced stiffness jump that has never been observed or exploited in other origami structures. The low stiffness during the folding stage offers an effective deploying and retraction mechanism with small actuation requirements; while the measured two orders of magnitude increase in stiffness at the self-locked stage provides the origami structure with high loading capacity. Note that although the experiments are performed on SC stacked units and blocks, all the self-locking sheets and blocks shown in Section 5 would possess similar stiffness jump properties.

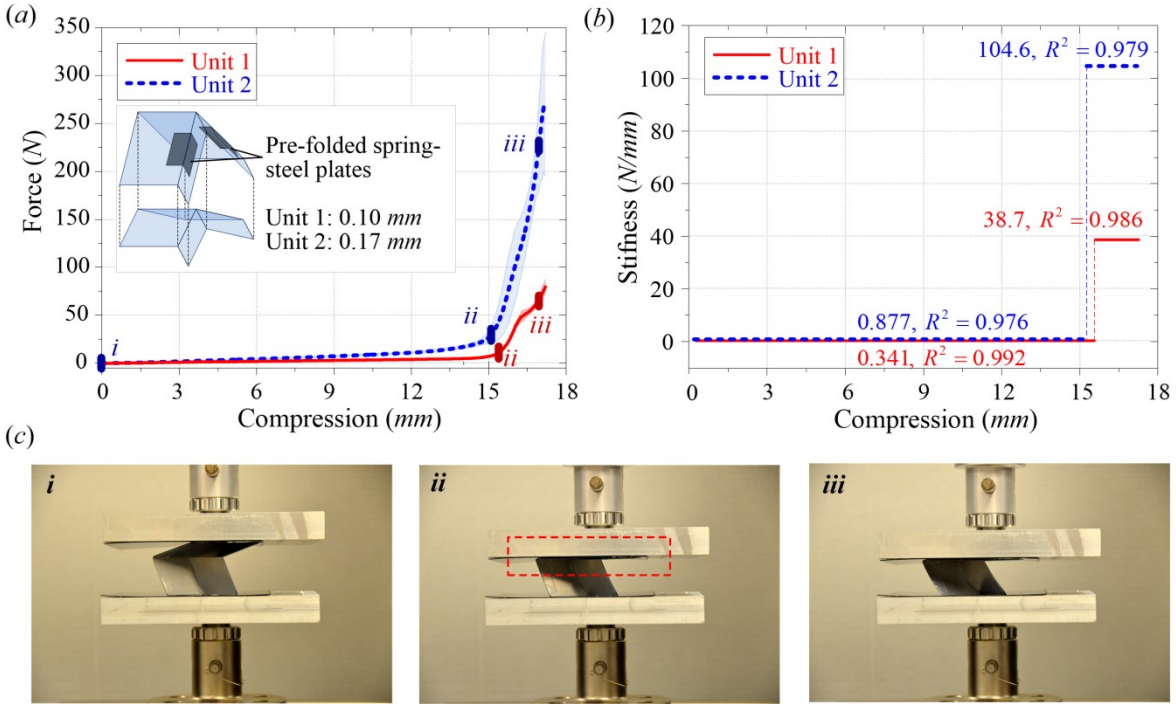


**Figure 12.** Separate compression tests on the two SC stacked units (nested-in configuration). (*a*) Force-displacement curves of the two units; inset shows the positions where spring-steel plates are pasted. (*b*) Stiffness obtained through linear regression, the stiffness values and the coefficient of determination ( $R^2$ ) are given. (*c*) Photos of a unit at three states *i*, *ii*, and *iii*; the binding facets at the self-locking instant *ii* are denoted by dashed rectangle.

## 8. Summary and Concluding remarks

This paper introduces a new category of origami structures with self-locking ability. We advance the state of the art by carrying out a comprehensive geometry and kinematic analysis on self-locking origami structures, and experimentally exploring their unique mechanical properties. The constituent units for such structure are different types of 4-vertex cell. In addition to and advancing from a single-component design, we incorporate two component cells (or stacked units) of the same type but with different geometry into the construction. We gain new knowledge and show that such two-component design produces a wide variety of sheets and blocks, making it suitable for different applications. Facet-binding provides the origami structures with self-locking ability, enabling them to stay at a pre-specified configuration without additional locking elements or actuators. Principles of achieving self-locking in

single-component and dual-component structures are illustrated via identifying the global binding folds that first close during folding.

By examining different cell tessellations, we reveal that the dual-component construction idea offers excellent programmability on the structures' kinematical properties, including the position and the number of flat-folded locking planes and locking points, and the deformation range. Such programmability cannot be achieved in single-component structures. In addition, the occurrence of self-locking can significantly affect the structure stiffness. Experiments demonstrate that the structure will experience a significant stiffness-jump and exhibit piecewise stiffness.

Given that the proposed and explored origami structures have such intriguing features as self-locking, programmable kinematical properties, and variable stiffness, they have great potential for scientific and engineering applications of various scales. For example, shape morphing [35] typically require a structure to change its shape between two targeted configurations with minimal actuation input, and then stay at the targeted shape while withstanding external loads. Such requirements can be achieved by tailoring the crease designs so that self-locking and the corresponding stiffness jump occur directly at the targeted load-bearing configurations. Locking induced stiffness jump can also be utilized as an embedded safety mechanism to prevent excessive deformations, which has many applications in robotic systems. Furthermore, structures with discrete stiffness jump display very rich nonlinear dynamic responses from harmonic excitations, so that self-locking origami can be developed into a foldable system with embedded vibration isolation or control functions [36,37]. Other than programmable deformation range and discrete stiffness jump, self-locking can enable other functionalities. For example, the contact of facets could significantly re-distribute the stress within the origami structure, therefore, self-locking could be exploited to reduce stress concentration from folding and improve the overall system durability and reliability [38,39].Moreover, although currently the self-locking behavior and locking-induced properties are passive, we envision that they can be transformed to be active if actuation mechanisms are included for folding. Available actuation methods include thermally-activation, chemically-activation, optically-activation, electrically-activation, and magnetically-activation (see review paper [2]); fluidic actuation [40–42] is also promising if the structure contains embedded tubular chambers.

Future research directions include development of passive and active self-locking origami-based metamaterials, investigation of the self-locking origami structures in terms of Lagrangian mechanics, self-locking origami dynamics, exploration of other types of structure with self-locking abilities (e.g., Hencky type structures[43,44]), and consideration of self-locking effects from the perspective of energy principles.

**Data accessibility.** The datasets supporting this article are already available in the article and the supplementary material themselves.

**Ethics.** The research work did not involve active collection of human data or any other ethical issues.

**Authors' contributions.** H.F. designed and conceived of the study, derived the equations, performed the analysis, carried out the experiments, and drafted the manuscript; S.L. checked all the equations, simulations, and experiment data, contributed to the simulations, and helped draft the manuscript; K.W.W. coordinated the research, supervised the study at all stages, and critically commented on the approach, results and manuscript. All authors gave final approval for publication.

**Competing interests.** The authors declare that they have no competing interests.

**Funding.** This research is partially supported by the National Science Foundation under Awards 1634545 and 1633952 and the University of Michigan Collegiate Professorship.

**Acknowledgements.** The authors thank the Referees for their helpful comments and suggestions.

# References


1. Lebée, A. 2015 From folds to structures, a review. *Int. J. Sp. Struct.* **30**, 55–74. (doi:10.1260/0266-3511.30.2.55)
2. Peraza-Hernandez, E. A., Hartl, D. J., Malak Jr, R. J. & Lagoudas, D. C. 2014 Origami-inspired active structures: a synthesis and review. *Smart Mater. Struct.* **23**, 94001. (doi:10.1088/0964-1726/23/9/094001)
3. Turner, N., Goodwine, B. & Sen, M. 2016 A review of origami applications in mechanical engineering. *Proc. Inst. Mech. Eng. Part C J. Mech. Eng. Sci.* **230**, 2345–2362. (doi:10.1177/0954406215597713)
4. Marras, A. E., Zhou, L., Su, H.-J. & Castro, C. E. 2015 Programmable motion of DNA origami mechanisms. *Proc. Natl. Acad. Sci.* **112**, 713–718. (doi:10.1073/pnas.1408869112)
5. Kuribayashi, K., Tsuchiya, K., You, Z., Tomus, D., Umemoto, M., Ito, T. & Sasaki, M. 2006 Self-deployable origami stent grafts as a biomedical application of Ni-rich TiNi shape memory alloy foil. *Mater. Sci. Eng. A* **419**, 131–137. (doi:10.1016/j.msea.2005.12.016)
6. Randall, C. L., Gultepe, E. & Gracias, D. H. 2012 Self-folding devices and materials for biomedical applications. *Trends Biotechnol.* **30**, 138–146. (doi:10.1016/j.tibtech.2011.06.013)
7. Felton, S., Tolley, M., Demaine, E., Rus, D. & Wood, R. 2014 A method for building self-folding machines. *Science (80-. ).* **345**, 644–646. (doi:10.1126/science.1252610)
8. Zhakypov, Z., Falahi, M., Shah, M. & Paik, J. 2015 The design and control of the multi-modal locomotion origami robot, Tribot. In *IEEE International Conference on Intelligent Robots and Systems*, pp. 4349–4355. Hamburg, Germany. (doi:10.1109/IROS.2015.7353994)
9. Gattas, J. M. & You, Z. 2015 Geometric assembly of rigid-foldable morphing sandwich structures. *Eng. Struct.* **94**, 149–159. (doi:10.1016/j.engstruct.2015.03.019)
10. Martinez, R. V, Fish, C. R., Chen, X. & Whitesides, G. M. 2012 Elastomeric origami: Programmable paper-elastomer composites as pneumatic actuators. *Adv. Funct. Mater.*
11. Schenk, M., Viquerat, A. D., Seffen, K. a. & Guest, S. D. 2014 Review of Inflatable Booms for Deployable Space Structures: Packing and Rigidization. *J. Spacecr. Rockets* **51**, 762–778. (doi:10.2514/1.A32598)
12. Reis, P. M., López Jiménez, F. & Marthelot, J. 2015 Transforming architectures inspired by origami. *Proc. Natl. Acad. Sci.* **112**, 201516974. (doi:10.1073/pnas.1516974112)
13. Filipov, E. T., Tachi, T. & Paulino, G. H. 2015 Origami tubes assembled into stiff, yet reconfigurable structures and metamaterials. *Proc. Natl. Acad. Sci.* **112**, 12321–12326. (doi:10.1073/pnas.1509465112)
14. Schenk, M. & Guest, S. D. 2013 Geometry of Miura-folded metamaterials. *Proc. Natl. Acad. Sci.* **110**, 3276–3281. (doi:10.1073/pnas.1217998110)
15. Yasuda, H. & Yang, J. 2015 Reentrant Origami-Based Metamaterials with Negative Poisson's Ratio and Bistability. *Phys. Rev. Lett.* **114**, 185502. (doi:10.1103/PhysRevLett.114.185502)
16. Silverberg, J. L., Evans, A. A., McLeod, L., Hayward, R. C., Hull, T., Santangelo, C. D. & Cohen, I. 2014 Using origami design principles to fold reprogrammable mechanical metamaterials. *Science (80-. ).* **345**, 647–650. (doi:10.1126/science.1252876)
17. Overvelde, J. T. B., Jong, T. A. De, Shevchenko, Y., Becerra, S. A., Whitesides, G. M., Weaver, J. C., Hoberman, C. & Bertoldi, K. 2016 A three-dimensional actuated origami-inspired transformable metamaterial with multiple degrees of freedom. *Nat. Commun.* **7**, 10929. (doi:10.1038/ncomms10929)
18. Waitukaitis, S., Menaut, R., Chen, B. G. & van Hecke, M. 2015 Origami Multistability: From Single

Vertices to Metasheets. *Phys. Rev. Lett.* **114**, 55503. (doi:10.1103/PhysRevLett.114.055503)

19. Silverberg, J. L., Na, J., Evans, A. A., Liu, B., Hull, T. C., Santangelo, C. D., Lang, R. J., Hayward, R. C. & Cohen, I. 2015 Origami structures with a critical transition to bistability arising from hidden degrees of freedom. *Nat. Mater.* **14**, 389–393. (doi:10.1038/NMAT4232)
20. Tachi, T. 2011 Rigid foldable thick origami. In *Origami 5*, pp. 253–264. CRC Press.
21. Edmondson, B. J., Lang, R. J., Magleby, S. P. & Howell, L. L. 2014 An offset panel technique for thick rigidly foldable origami. In *Proceedings of the ASME 2014 International Design Engineering Technical Conferences & Computers and Information in Engineering Conference (IDETC/CIE 2014)*, pp. DETC2014-35606. Buffalo, New York, USA: ASME.
22. Chen, Y., Peng, R. & You, Z. 2015 Origami of thick panels. *Science (80-. ).* **349**, 396–400.
23. Deng, D. & Chen, Y. 2014 Origami-Based Self-Folding Structure Design and Fabrication Using Projection Based Stereolithography. *J. Mech. Des.* **137**, 21701. (doi:10.1115/1.4029066)
24. Leong, T. G., Lester, P. A., Koh, T. L., Call, E. K. & Gracias, D. H. 2007 Surface Tension-Driven Self-Folding Polyhedra. *Langmuir* **23**, 8747–8751.
25. Felton, S. M., Tolley, M. T., Shin, B., Onal, C. D., Demaine, E. D., Rus, D. & Wood, R. J. 2013 Self-folding with shape memory composites. *Soft Matter* **9**, 7688–7694. (doi:10.1039/C3SM51003D)
26. Saunders, R., Hartl, D., Malak, R. & Lagoudas, D. 2014 Design and analysis of a self-folding sma-smp composite laminate. In *Proceedings of the ASME 2014 International Design Engineering Technical Conferences & Computers and Information in Engineering Conference (IDETC/CIE 2014)*, pp. DETC2014-35151. Buffalo: ASME.
27. Waitukaitis, S. & van Hecke, M. 2016 Origami building blocks: generic and special 4-vertices. *Phys. Rev. E* **93**, 23003.
28. Hull, T. 2013 *Project origami: activities for exploring mathematics*. 2nd edn. Boca Raton: CRC Press.
29. Fang, H., Li, S., Xu, J. & Wang, K. W. 2016 Locking mechanisms in degree-4 vertex origami structures. *Proc. SPIE 9799 Act. Passiv. Smart Struct. Integr. Syst.* **1**, 979910. (doi:10.1117/12.2217592)
30. Fang, H., Li, S., Ji, H. & Wang, K. W. 2016 Uncovering the deformation mechanisms of origami metamaterials by introducing generic degree-4 vertices. *Phys. Rev. E*
31. Li, S. & Wang, K. W. 2015 Fluidic origami cellular structure – Combining the plant nastic movements with paper folding art. In *Proc. SPIE 9431, Active and Passive Smart Structures and Integrated Systems 2015* (ed Wei-Hsin Liao), pp. 94310H. SPIE. (doi:10.1117/12.2082888)
32. Lv, C., Krishnaraju, D., Konjevod, G., Yu, H. & Jiang, H. 2014 Origami based Mechanical Metamaterials. *Sci. Rep.* **4**, 5979. (doi:10.1038/srep05979)
33. Ma, J. & You, Z. 2013 Energy Absorption of Thin-Walled Square Tubes With a Prefolded Origami Pattern—Part I: Geometry and Numerical Simulation. *J. Appl. Mech.* **81**, 11003. (doi:10.1115/1.4024405)
34. Song, J., Chen, Y. & Lu, G. 2012 Axial crushing of thin-walled structures with origami patterns. *Thin-Walled Struct.* **54**, 65–71. (doi:10.1016/j.tws.2012.02.007)
35. Kuder, I. K., Arrieta, A. F., Raither, W. E. & Ermanni, P. 2013 Variable stiffness material and structural concepts for morphing applications. *Prog. Aerosp. Sci.* **63**, 33–55. (doi:10.1016/j.paerosci.2013.07.001)
36. Running, D. M., Ligon, J. B. & Miskioglu, I. 2004 Frequency response of a piecewise linear vibration isolator. *J. Vib. Control* **10**, 1775–1794.
37. Araki, Y., Asai, T. & Masui, T. 2009 Vertical vibration isolator having piecewise-constant restoring force.

*Earthq. Eng. Struct. Dyn.* **39**, 1505–1523. (doi:10.1002/eqe)

38. Cirone, S. a., Hayes, G. R., Babcox, B. L., Frecker, M., Adair, J. H. & Lesieutre, G. a. 2012 Design of contact-aided compliant cellular mechanisms with curved walls. *J. Intell. Mater. Syst. Struct.* **23**, 1773–1785. (doi:10.1117/12.880529)
39. Mehta, V., Frecker, M. & Lesieutre, G. A. 2009 Stress Relief in Contact-Aided Compliant Cellular Mechanisms. *J. Mech. Des.* **131**, 91009. (doi:10.1115/1.3165778)
40. Li, S. & Wang, K. W. 2015 Fluidic origami: a plant-inspired adaptive structure with shape morphing and stiffness tuning. *Smart Mater. Struct.* **24**, 105031. (doi:10.1088/0964-1726/24/10/105031)
41. Li, S. & Wang, K. W. 2015 Fluidic origami with embedded pressure dependent multi-stability: a plant inspired innovation. *J. R. Soc. Interface* **12**, 20150639.
42. Li, S., Fang, H. & Wang, K. W. 2016 Recoverable and programmable collapse from folding pressurized origami cellular solids. *Phys. Rev. Lett.* **117**, 114301. (doi:10.1103/PhysRevLett.117.114301)
43. Dell'Isola, F., Giorgio, I., Pawlikowski, M. & Rizzi, N. L. 2016 Large deformations of planar extensible beams and pantographic lattices: heuristic homogenization, experimental and numerical examples of equilibrium. *Proc. R. Soc. A Math. Phys. Eng. Sci.* **472**, 20150790. (doi:10.1098/rspa.2015.0790)
44. Turco, E., dell'Isola, F., Cazzani, A. & Rizzi, N. L. 2016 Hencky-type discrete model for pantographic structures: numerical comparison with second gradient continuum models. *Zeitschrift fur Angew. Math. und Phys.* **67**, 1–28. (doi:10.1007/s00033-016-0681-8)